Electronic Supplementary Material (ESI) for Physical Chemistry Chemical Physics.

Supporting Information:

Ultrafast dynamics of fluorene initiated by highly intense laser fields

Contents

1 Mass-spectrum of fluorene

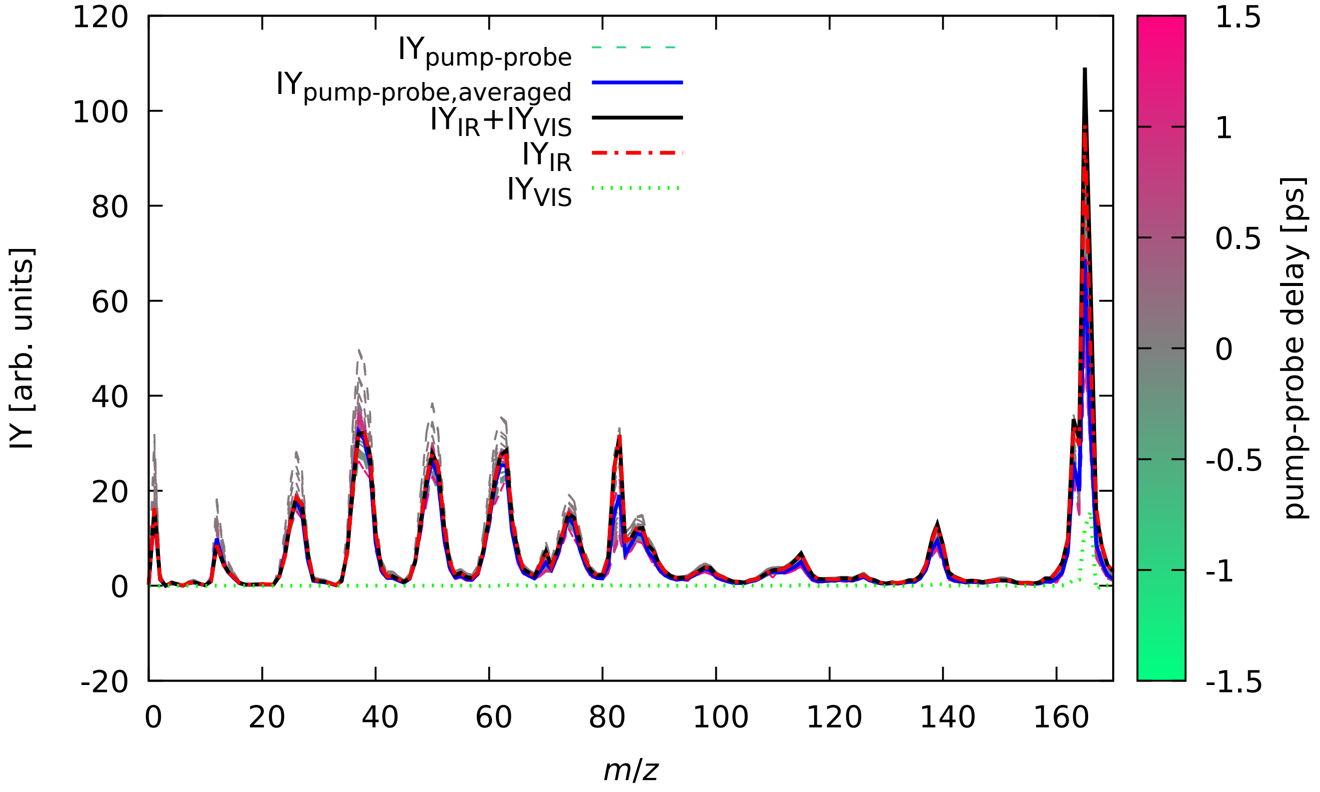

Figure S1 Mass spectra (MS) of FLU in various experiment and averaging regimes. $\mathrm{IY}_{\mathrm{pump-probe}}$ shows the individual MS at given pump-probe delays with delay value shown with color grading from green to pink. $\mathrm{IY}_{\mathrm{pump-probe,averaged}}$ is the MS obtained by averaging over all pump-probe delays, $\mathrm{IY}_{\mathrm{IR}}$ and $\mathrm{IY}_{\mathrm{VIS}}$ are the pump-only and probe-only MS, and $\mathrm{IY}_{\mathrm{IR}} + \mathrm{IY}_{\mathrm{VIS}}$ is a sum of these MS, used as a background in further discussion.

Local discrepancy estimator for the pump-probe MS $I^{(\mathrm{IR-VIS})}(m/z,t)$ for a given point of m/z and pump-probe delay t from reference pump-only MS $I^{(\mathrm{IR})}(m/z)$ we define as follows:

$$D(m/z,t) = 100\% \cdot \overbrace{\frac{|I^{(\mathrm{IR})}(m/z)|}{\sum_{m/z} |I^{(\mathrm{IR})}(m/z)|}}^{D_1} \cdot \overbrace{\sqrt{\frac{\left(I^{(\mathrm{IR})}(m/z) - I^{(\mathrm{IR-VIS})}(m/z,t)\right)^2}{I^{(\mathrm{IR})}(m/z)^2}}}^{D_2} = \\ = 100\% \cdot \frac{|I^{(\mathrm{IR})}(m/z) - I^{(\mathrm{IR-VIS})}(m/z,t)|}{\sum_{m/z} |I^{(\mathrm{IR})}(m/z)|}\ . \qquad (1)$$

Here, the first multiplier (D_1) characterizes the contribution of a given peak in the total mass spectrum (to damp contributions from the near-zero-intensity regions), and the second multiplier characterizes the deviation of MS intensity at a given m/z and t values from the corresponding IR-only number at a given m/z. An illustration of this estimator is provided in Figure S4. The

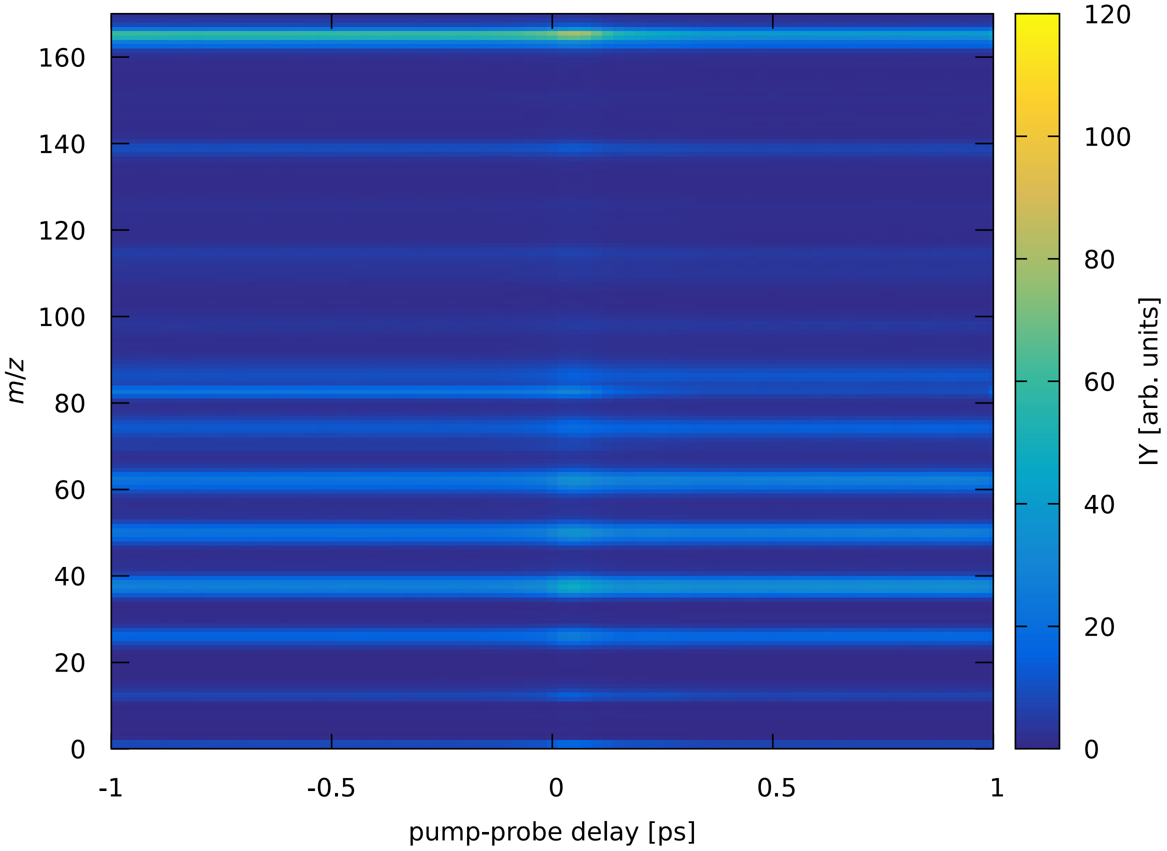

Figure S2 Pump-probe dependent mass spectrum of FLU in the full range of m/z.

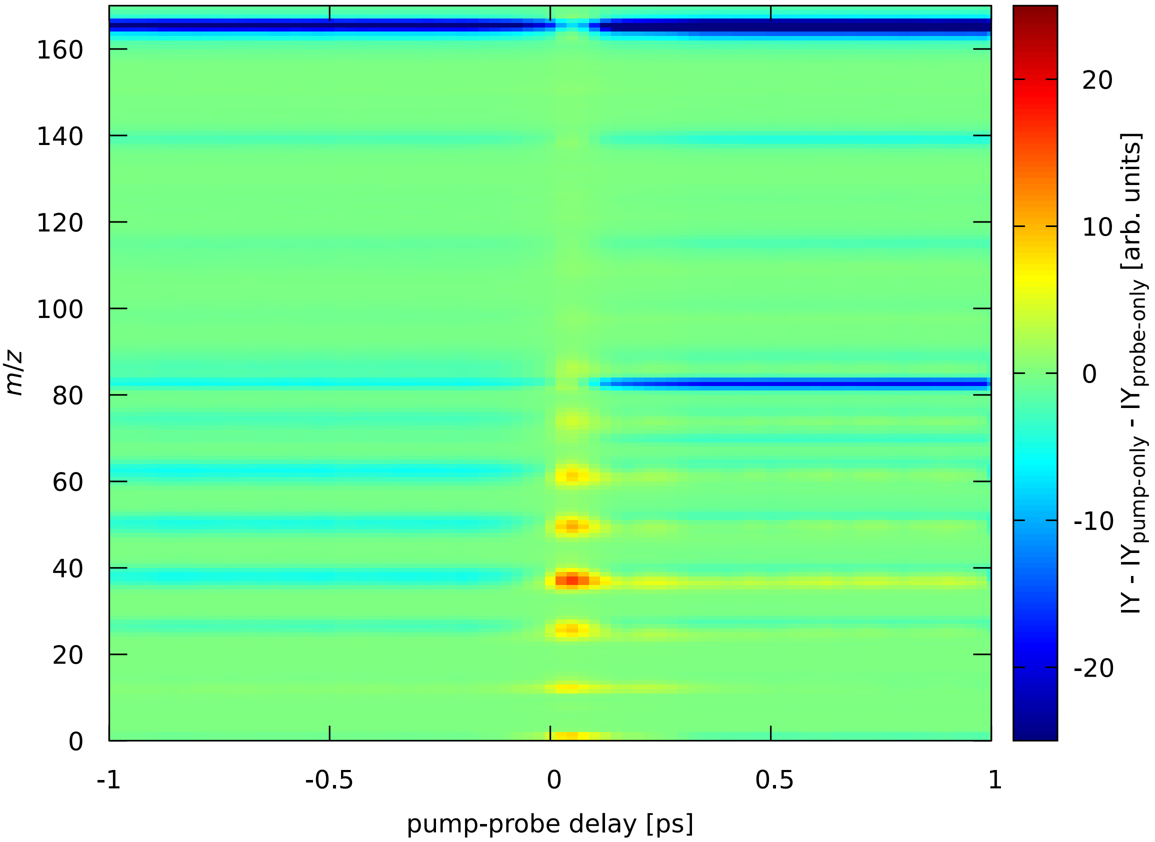

Figure S3 Pump-probe dependent mass spectrum of FLU in the full range of m/z with subtracted pump-only and probe-only background. This is the full-range version of the Figure 7a of the manuscript.

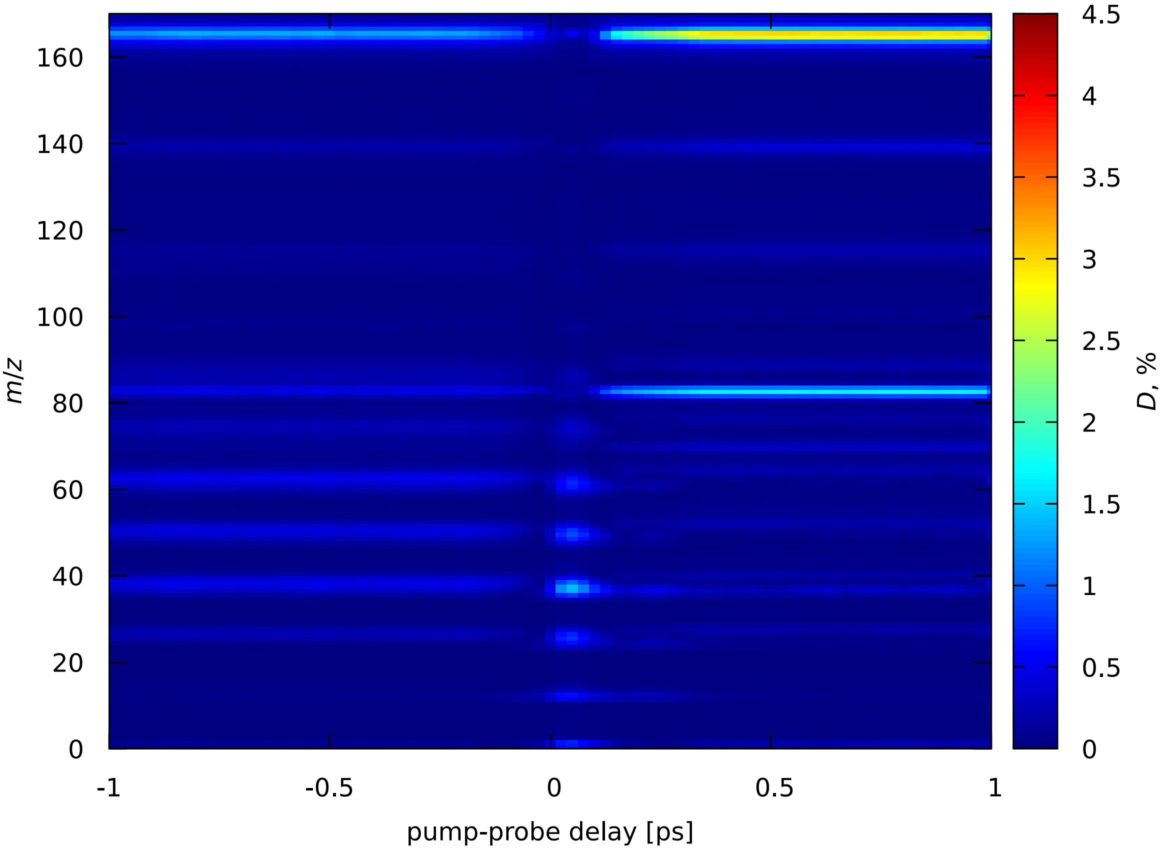

Figure S4 Pump-probe dependent local discrepancy estimator (Equation 1) of FLU in the full range of m/z.

2 Recoil frame covariance analysis

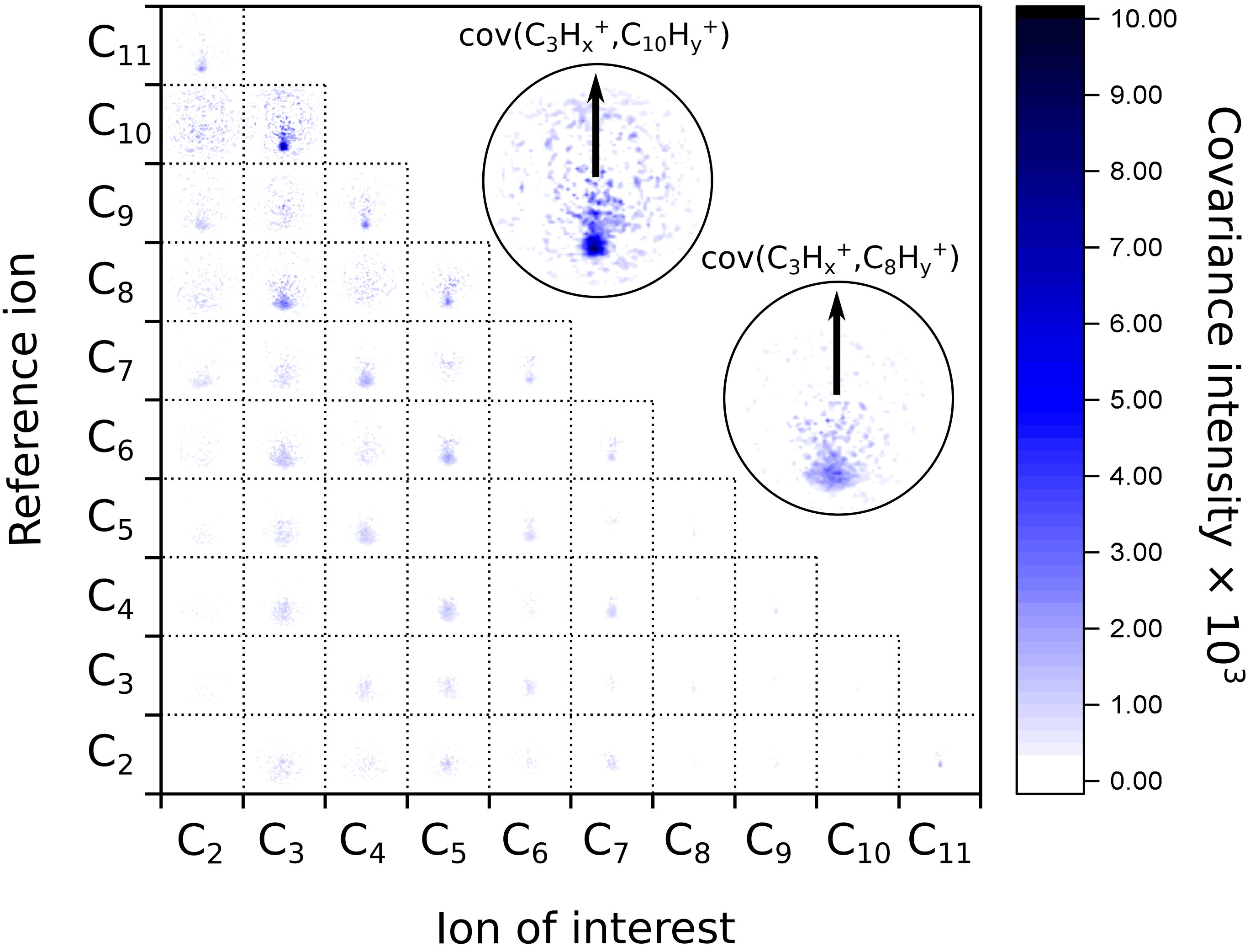

Figure S5 Matrix of the recoil frame covariance images for different pairs of the recoiling ions. The two insets show zoomed images of the $C_3H_x{}^+$ ion of interest recoiling against $C_{10}H_y{}^+$ and $C_8H_y{}^+$ reference ions. The arrows in both insets show the reference ion direction for all the recoil frame covariance images. This is the enlarged Figure 3 of the manuscript.

3 Pump pulse characterization

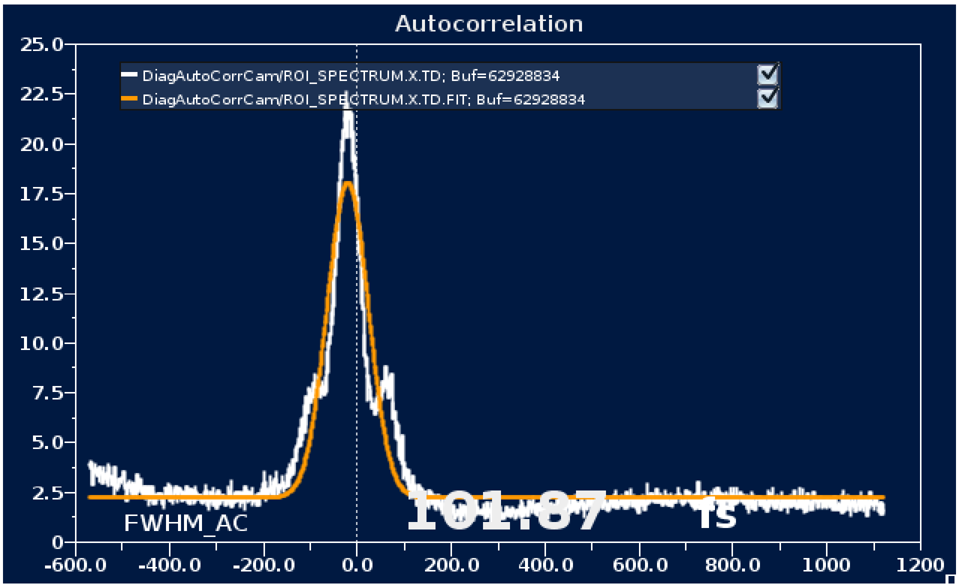

Figure S6 Snapshot from the beamtime F-20170540 logbook. Single shot autocorrelation measurement of IR laser pulse. The white trace denotes the measured signal, and the yellow curve presents a Gaussian fit. The x-axis is the (uncalibrated) delay in fs, y-axis is the intensity in arbitrary units.

To estimate the peak power of the laser pulses, we use Gaussian approximation to the reaction profile:

$$I(x,y,t) = I_0 \cdot \exp\left(-\frac{t^2}{2\sigma_t^2} - \frac{(x^2+y^2)}{2\sigma_r^2}\right) \ , \tag{2}$$

where $I(x,y,t)$ is the intensity at time t at the position of x,y in a plane, orthogonal to the pulse propagation direction, σ_t is the temporal width of the pulse, σ_r is the radial width of the pulse in xy-plane, and I_0 is the peak power of the pulse. In SI units, I and I_0 are given in [W/m^2], σ_t is given in [s], and σ_r is given in [m]. During the experiment, we measure the pulse energy (E_pulse) with a photodiode. It is related to the intensity I as

$$E_\text{pulse} = \iiint\limits_{-\infty}^{+\infty} I(x,y,t)dxdydt = (2\pi)^{3/2} \cdot \sigma_t \cdot \sigma_r^2 \cdot I_0 \ . \tag{3}$$

The widths σ_t and σ_r are related to the corresponding full width at half maximum (FWHM) values as $\text{FWHM}_q = 2\sqrt{2\ln(2)}\sigma_q$ $(q = t, r)$. From this, we can get the peak intensity according to the formula

$$I_0 = 8 \cdot \left(\frac{\ln(2)}{\pi}\right)^{3/2} \frac{E_\text{pulse}}{\text{FWHM}_t \cdot \text{FWHM}_r^2} \ . \tag{4}$$

The focal size was estimated to be $\text{FWHM}_r = 60$ [μm], the pulse duration in beamtime F-20170540 (in 2018) was $\text{FWHM}_t = 60$ [fs], while in beamtime F-20211752 (in 2023) it was $\text{FWHM}_t = 55$ [fs]. In

Table S1 Measured pulse energies (E_{pulse}) and corresponding peak intensities (I_0) of attenuated pulses in beamtime F-20211752. Attenuation done by filters with different transmissions (first column).

Transmission	E_{pulse} [μJ]	I_0 [W/cm^2]
0.3	35	1.5×10^{13}
0.4	58	2.4×10^{13}
0.5	83	3.5×10^{13}
0.6	107	4.5×10^{13}
0.7	130	5.4×10^{13}
0.8	143	6.0×10^{13}
0.9	163	6.8×10^{13}

the pump-probe measurements (done in 2018), the measured IR pulse energy was $E_{\text{pulse}} = 85$ [μJ],[S1] which gives an estimation of the peak power of $I_0 = 3.3 \times 10^{13}$ [W/cm^2]. In the laser power scan (performed in 2023), which was done by varying the transmission of the pulse by the filters, the measured pulse energies and corresponding peak powers are given in Table S1.

4 Fitting of the pump-probe-dependent data

4.1 General note

In the following section, the pump-probe fit results are presented. Every dataset has a feature that appears from the double peak feature of the pump and probe pulses. This feature can be seen in the autocorrelation measurements of the laser pulse shape (Figure S6). The autocorrelation is a symmetric function, so the pre- or post-pulse feature appears from both sides of the central peak in Figure S6. Since pump and probe pulses are produced from the same laser pulse, they also show this autocorrelation feature in all resulting fragments. Due to the complicated nature of such a fit, we treated the cross-correlation as an effective Gaussian function (similar to that in Figure S6). To ensure that no overfitting of this feature occurs, we controlled the residuals of the fit, which should have been showing the unfitted shoulders. More details on that can be found in Ref. S1.

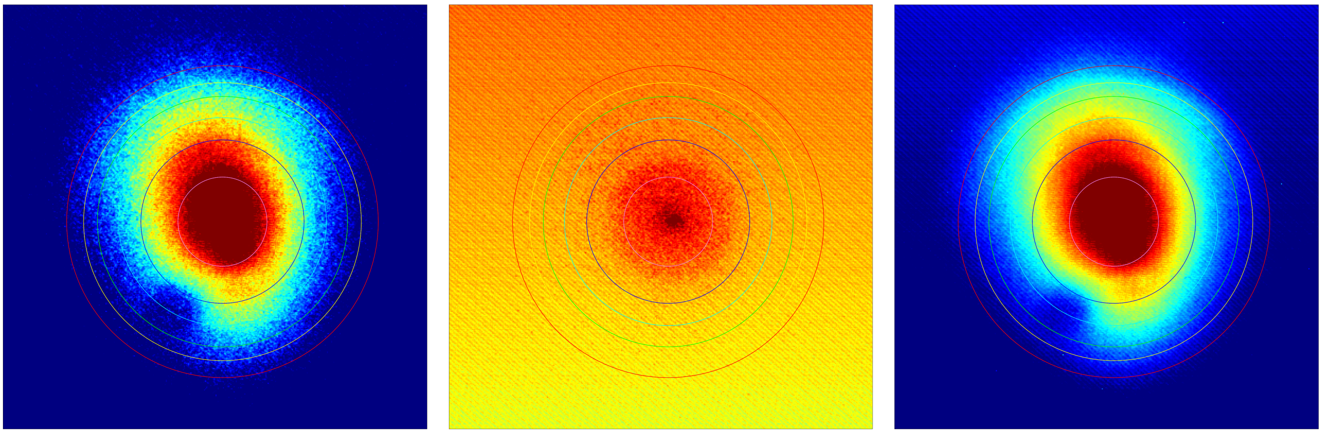

Figure S7 Comparison of the electron VMI images of FLU in (from left to right) IR-only, VIS-only, and pump-probe IR-VIS regime with averaging over all pump-probe delays. The circles show the expected positions of the ATI peaks.

The general description of the fitting procedure with (MC)^{3}Fitting code[S2] can be found in Ref. S3. The details about the models applied to this specific dataset can be found in the Ph.D. theses of Pragya Chopra and Diksha Garg.[S1,S4] During the preliminary fits, various models were tried out, in which three different cases were considered:[S1]

- dynamics is only pumped by the IR pulse and only probed with the VIS pulse;
- dynamics is only pumped by the VIS pulse and only probed with the IR pulse;
- dynamics is pumped and probed by both the IR and VIS pulses.

Only the first case scenario allowed the data to be described consistently. This is supported by comparing the IR-only and VIS-only MS and electron VMI images with the IR-VIS pump-probe results, averaged over all pump-probe delays (Figures S1, S7). As one can see, the MS of the IR-only and IR-VIS are very similar, whether the VIS-only spectrum is visibly different from both the IR-only and IR-VIS with only parent ions present. To quantify the similarity of the VIS-only and IR-VIS, we calculated the R_f deviation of VIS-only and IR-VIS spectrum from IR-only data according to the expression

$$R_f = 100\% \times \sqrt{\frac{\sum_i \left(I_i^{(\mathrm{IR})} - I_i^{(\mathrm{X})}\right)^2}{\sum_i \left(I_i^{(\mathrm{IR})}\right)^2}} ,$$

where I_i is the MS value of the dataset from Figure S1 indicated with the upper index (with $\mathrm{X} = \mathrm{VIS}, \mathrm{IR} - \mathrm{VIS}$), and the lower index i enumerating the integer m/z values. For IR-VIS, this gave $R_f = 24$ %, whereas, for VIS-only, the same parameter was $R_f = 93$ %. In other words, the spectra of the IR-only and IR-VIS data are different by only 24 %, whereas for the VIS-only, the similarity is much lower. The same trend is seen in the electron VMI images (Figure S5): IR-only and IR-VIS spectra show similar ATI features, whether VIS-only shows only a zero-kinetic energy peak in the center with a single ring around. Such comparison of the IR-only, VIS-only, and IR-VIS datasets also justifies the static analysis we performed since the total pump-probe effect averaged over all m/z values is estimated to be only around 24 % of the data (according to the R_f values for MS).

4.2 Parent species

Table S2 The relaxation lifetimes of the parent ions. Cross-correlation times τ_{cc} are related to the FWHM as $\tau_{\mathrm{cc}} = \mathrm{FWHM}/(2\sqrt{\ln(2)}) \approx 0.6 \cdot \mathrm{FWHM}$.

Specie	Channel	τ_{cc} (fs)	transient peak lifetime (fs)
$C_{13}H_{10}^{+}$	-	63±1	62±1
$C_{13}H_{10}^{2+}$	-	23±1	79±1
$C_{13}H_{10}^{3+}$	-	85±7	42±6
$C_{13}H_{9}^{+}$	-	48±1	91±1

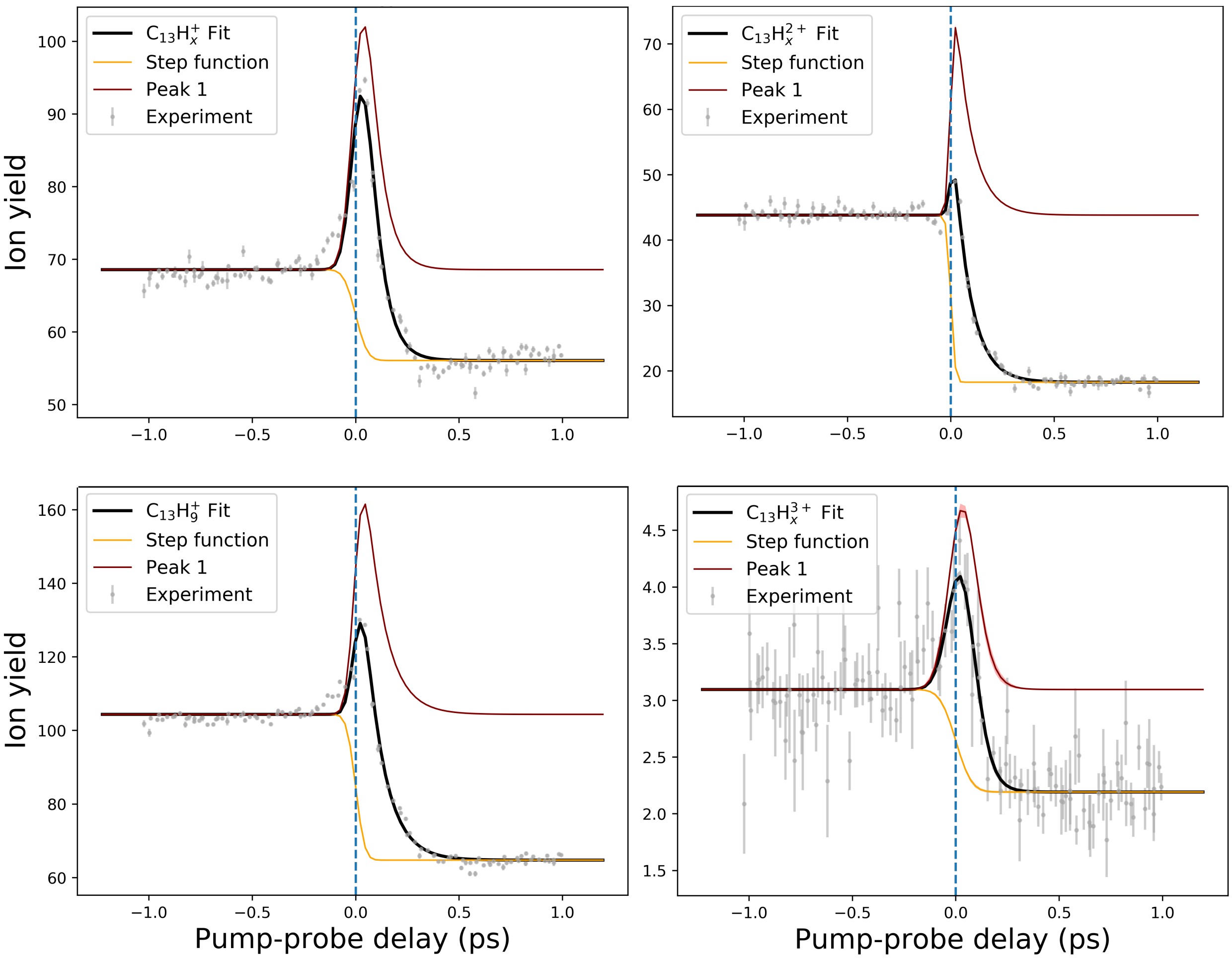

Figure S8 Fitted parent ion yields

4.3 Small fragment ions

Table S3 The relaxation lifetimes of the small fragment ions. Cross-correlation times τ_{cc} are related to the FWHM as $\tau_{\mathrm{cc}} = \mathrm{FWHM}/(2\sqrt{\ln(2)}) \approx 0.6 \cdot \mathrm{FWHM}$.

Specie	Channel	τ_{cc} (fs)	transient peak lifetime (fs)
CH_x^+	(1,0)	65±5	2±1* (peak 1) 262±5 (peak 2)
	(1,1)	125±4	51±5
	(1,2)	110±9	20±5
$C_2H_x^+$	(1,0)	64±3	10±2 (peak 1) 452±10 (peak 2)
	(1,1)	71±3	23±2
	(1,2)	68±2	20±2
$C_3H_x^+$	(1,0)	63±3	12±2 (peak 1) 966±16 (peak 2)
	(1,1)	66±3	19±2
	(1,2)	65±4	20±2
$C_4H_x^+$	(1,0)	61±3	14±2 (peak 1) 460±5 (peak 2)
	(1,1)	70±3	26±2
	(1,2)	66±2	22±2
$C_5H_x^+$	(1,0)	62±3	15±2 (peak 1) 239±17 (peak 2)
	(1,1)	79±4	35±2
	(1,2)	68±3	28±2
$C_6H_x^+$	(1,0)	60±4	16±2 (peak 1) 251±9 (peak 2)
	(1,1)	88±4	45±3
	(1,2)	66±3	35±2
$C_7H_x^+$	(1,0)	57±3	9±3 (peak 1) 638±9 (peak 2)
	(1,1)	79±4	59±3
	(1,2)	64±3	44±3
$C_8H_x^+$	(1,0)	70±6	12±4 (peak 1) 128±10 (peak 2)
	(1,1)	83±6	58±4
	(1,2)	71±5	49±4

* – this lifetime is more than 10 times smaller than the corresponding τ_{cc}, which means that this is effectively an instantaneous process that could not be resolved within the current experiment.

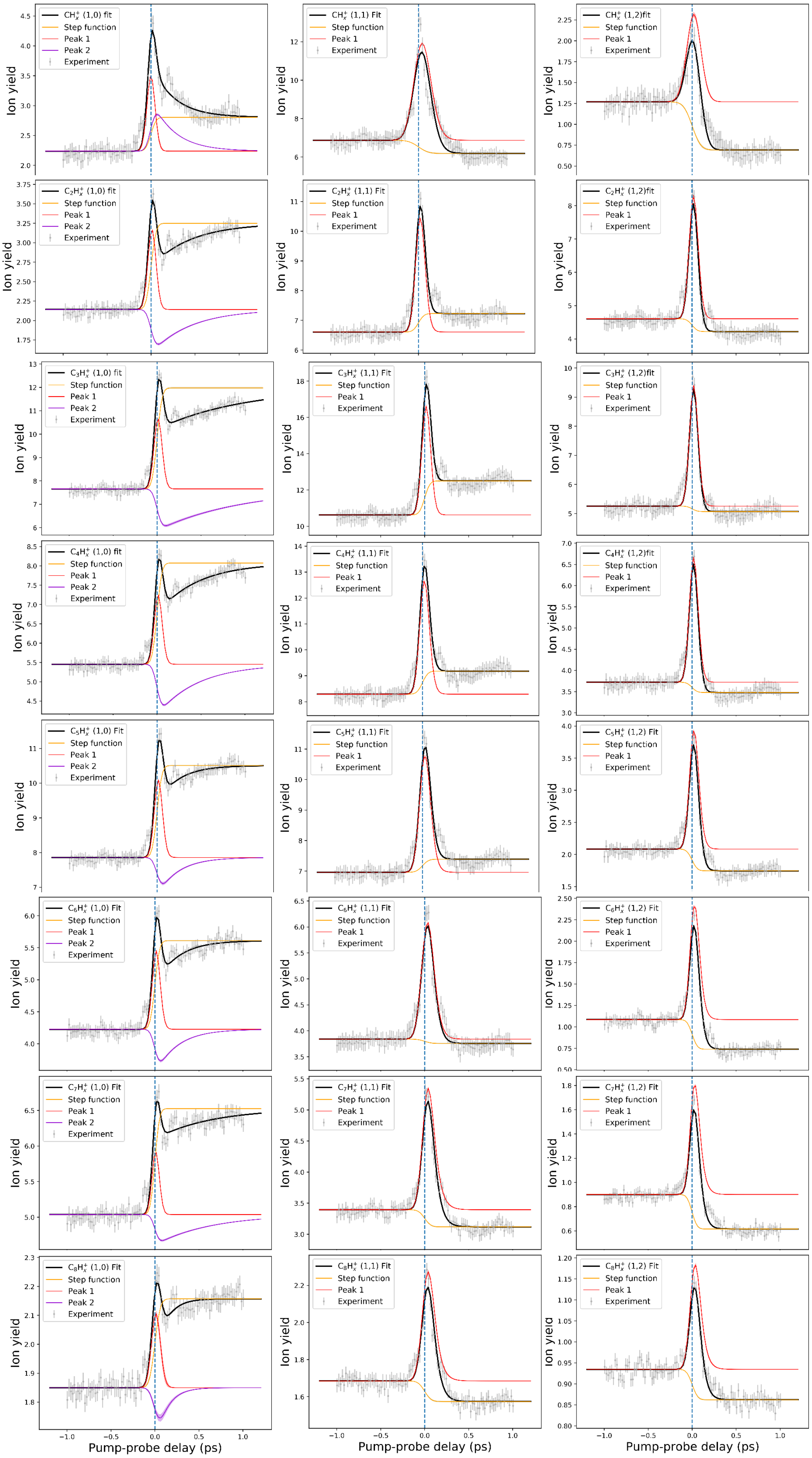

Figure S9 Fitted momentum-separated ion yields of small ionic fragments.

4.4 Large fragment ions

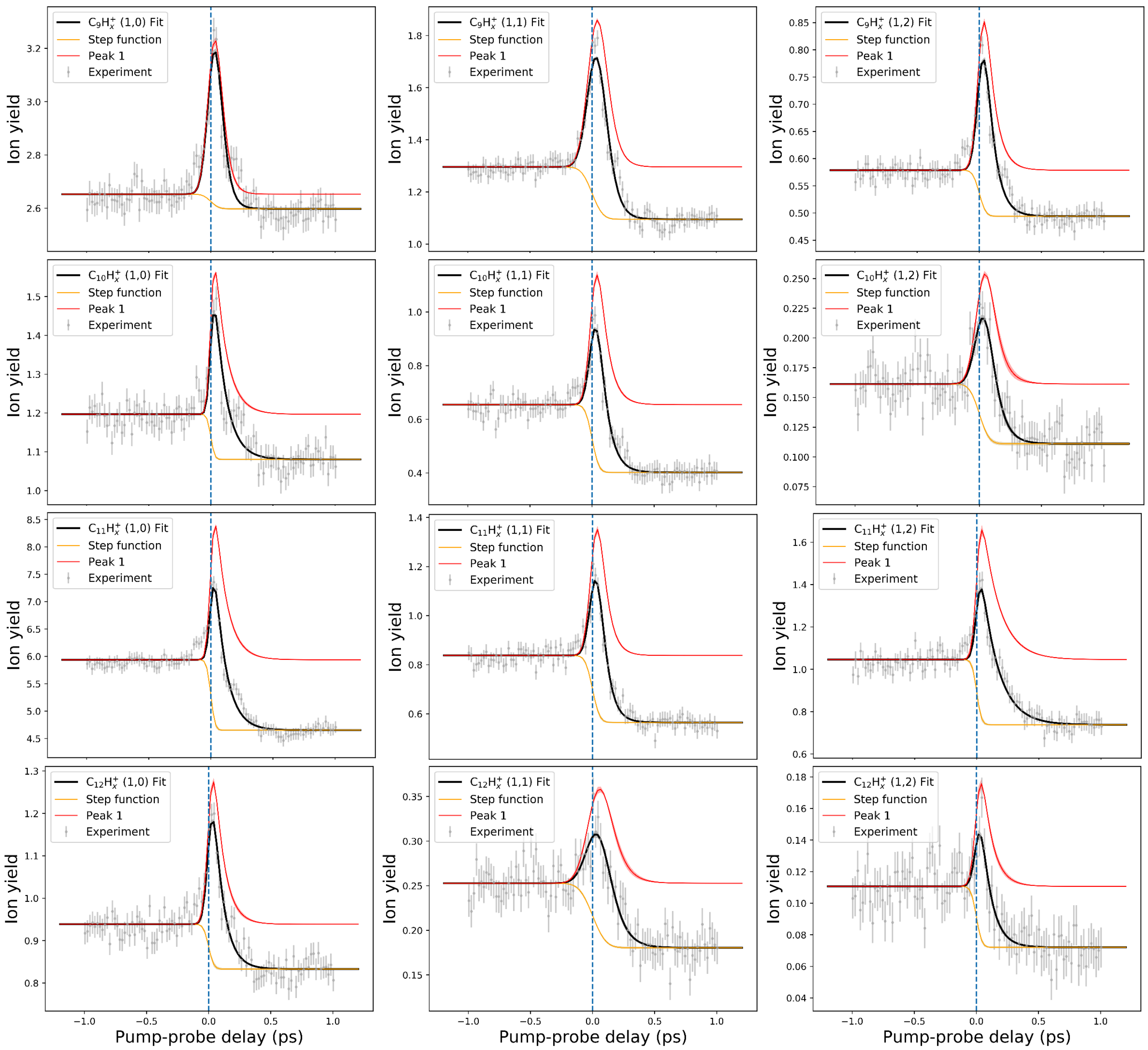

Figure S10 Fitted momentum-separated ion yields of large ionic fragments.

Table S4 The relaxation lifetimes of the large fragment ions. Cross-correlation times τ_{cc} are related to the FWHM as $\tau_{\mathrm{cc}} = \mathrm{FWHM}/(2\sqrt{\ln(2)}) \approx 0.6 \cdot \mathrm{FWHM}$.

Specie	Channel	τ_{cc} (fs)	transient peak lifetime (fs)
$C_9H_x^+$	(1,0)	71±6	46±4
	(1,1)	96±4	58±3
	(1,2)	59±6	71±4
$C_{10}H_x^+$	(1,0)	35±4	92±6
	(1,1)	62±7	70±5
	(1,2)	88±7	72±12
$C_{11}H_x^+$	(1,0)	38±5	92±6
	(1,1)	65±7	62±5
	(1,2)	43±8	136±6
$C_{12}H_x^+$	(1,0)	47±8	79±7
	(1,1)	119±10	84±8
	(1,2)	50±8	81±8

4.5 Dicationic fragment ions

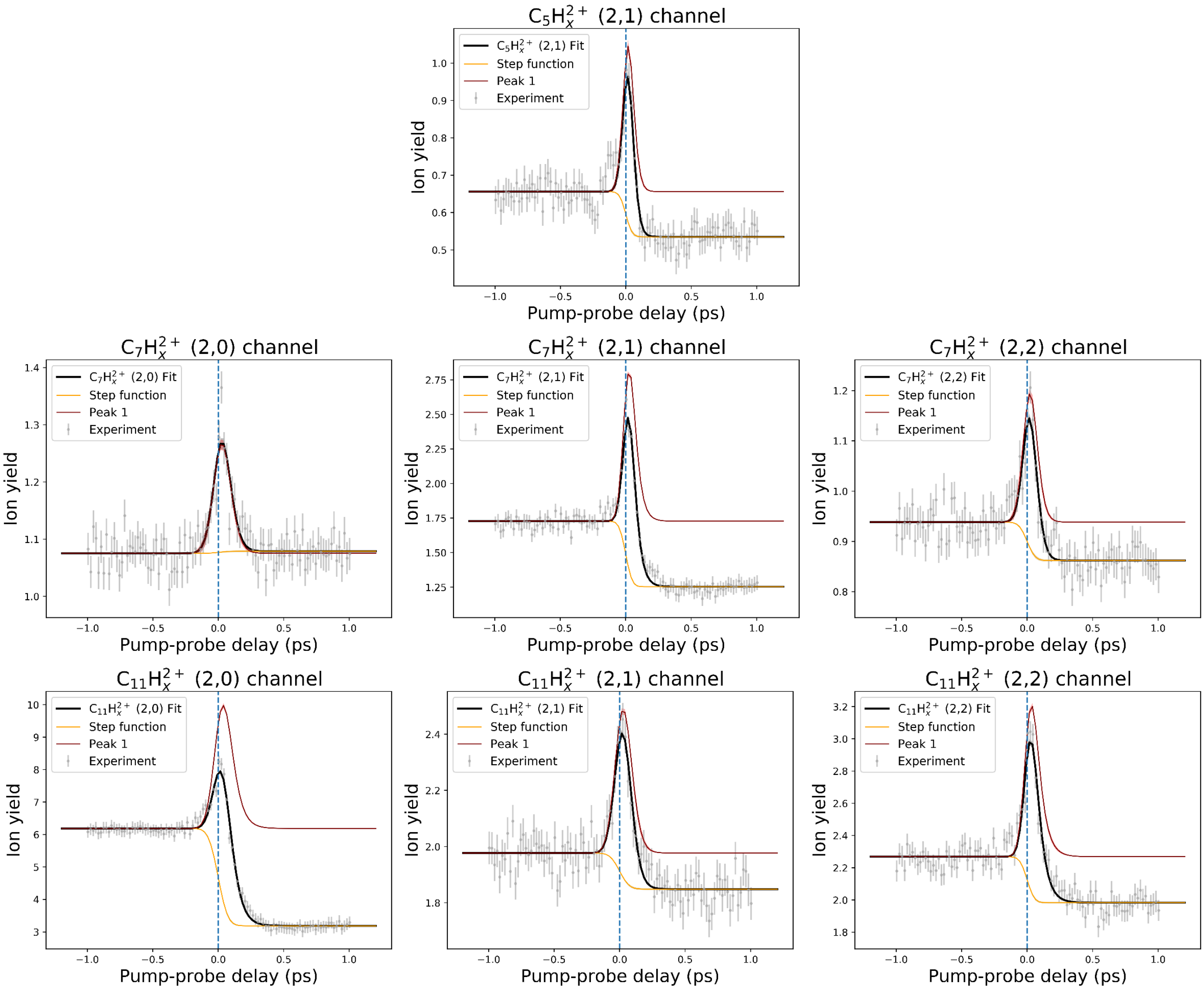

Figure S11 Fitted momentum-separated ion yields of dicationic fragments.

Table S5 The relaxation lifetimes of the dicationic fragments. Cross-correlation times τ_{cc} are related to the FWHM as $\tau =_{\mathrm{cc}} \mathrm{FWHM}/(2\sqrt{\ln(2)}) \approx 0.6 \cdot \mathrm{FWHM}$.

Specie	Channel	τ_{cc} (fs)	transient peak lifetime (fs)
$C_5H_x^{2+}$	(2,1)	53±6	22±4
$C_7H_x^{2+}$	(2,0)	86±12	34±7
	(2,1)	55±3	38±2
	(2,2)	70±9	27±6
$C_{11}H_x^{2+}$	(2,0)	82±4	53±3
	(2,1)	82±5	34±5
	(2,2)	62±5	52±4

4.6 Electron data

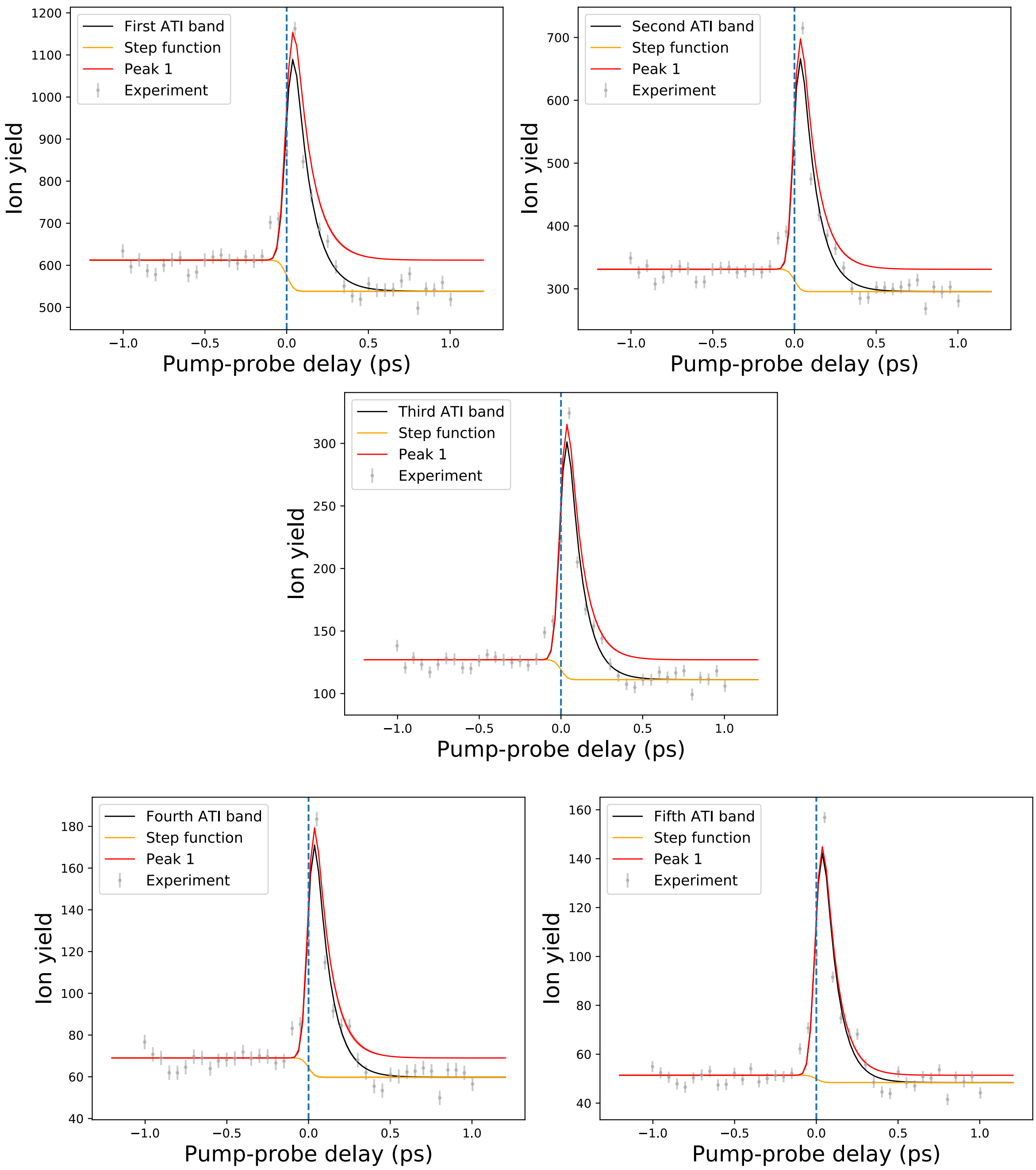

Figure S12 Fitted electron yields from photoelectron spectra.

Table S6 The relaxation lifetimes of the features in the photoelectron spectra. Cross-correlation times τ_{cc} are related to the FWHM as $\tau_{\mathrm{cc}} = \mathrm{FWHM}/(2\sqrt{\ln(2)}) \approx 0.6 \cdot \mathrm{FWHM}$.

Specie	Channel	τ_{cc} (fs)	transient peak lifetime (fs)
e^-	1-st ATI band	48±3	102±4
	2-st ATI band	42±3	93±3
	3-st ATI band	44±2	87±3
	4-st ATI band	42±3	90±5
	5-st ATI band	46±2	83±3

5 ATI spectrum analysis

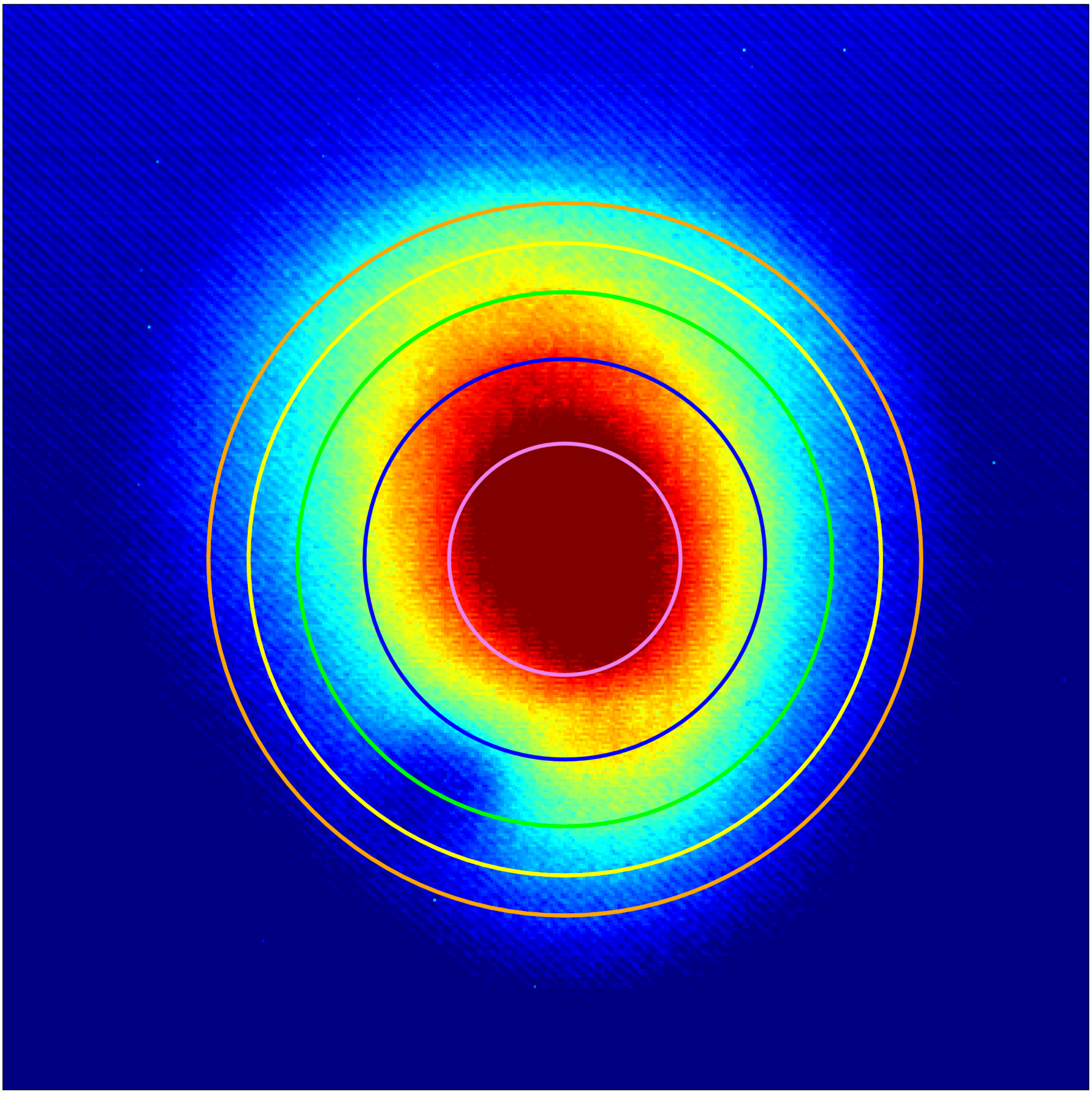

Figure S13 Example of the electron image from a single run with circles indicated ATI features identified from the angular-integrated electron yields

The center of the electron velocity map images (eVMI) and the kinetic energy calibration were found using the He II line feature, visible in the XUV-initiated experiments performed before and after the collection of the IR-VIS data.

After angular integration of eVMI, the radial yields of the electrons were Abel-inverted, and the

Table S7 Parameters of the fit (Equation 5) of the EY spectrum.

ATI peak order (k)	Parameter	Value
1	A_0 [arb. units]	27.2 ± 0.3
	E_0 [eV]	0.763 ± 0.008
	σ_0 [eV]	0.58 ± 0.02
2	A_1 [arb. units]	17.2 ± 0.2
	E_1 [eV]	2.29 ± 0.02
	σ_1 [eV]	0.88 ± 0.05
3	A_2 [arb. units]	8.4 ± 0.3
	E_2 [eV]	4.07 ± 0.04
	σ_2 [eV]	0.8 ± 0.1
4	A_3 [arb. units]	5.2 ± 0.9
	E_3 [eV]	5.70 ± 0.08
	σ_3 [eV]	0.7 ± 0.1
5	A_4 [arb. units]	4.5 ± 0.3
	E_4 [eV]	7.2 ± 0.2
	σ_4 [eV]	1.2 ± 0.2

resulting electron yield (EY) spectrum was fitted with a sum of Gaussian functions as

$$\mathrm{EY}(E) = \sum_{k=0}^{4} A_k \cdot \exp\left(-\frac{(E-E_k)^2}{2\sigma_k^2}\right) , \tag{5}$$

where E is the electron kinetic energy derived from the radial coordinate r of the EY as $E = E_{\mathrm{He\ II}} \cdot (r/r_{\mathrm{He\ II}})^2$, where $E_{\mathrm{He\ II}} = h\nu_{\mathrm{XUV}} - \mathrm{IP}_{\mathrm{He}}$ is the kinetic energy of electrons, corresponding to the He II line obtained with XUV photons of energy $h\nu_{\mathrm{XUV}} \approx 41$ [eV], that were used in calibration experiments, $\mathrm{IP}_{\mathrm{He}} \approx 25$ [eV] is the first ionization potential of helium, and $r_{\mathrm{He\ II}}$ was the position of the He II line feature in our calibration spectra. The resulting fitted parameters of Equation 5 and the fitted dependencies are given in Table S7.

The work function was obtained by fitting the resulting positions of the ATI peaks into the equation

$$E_k = h\nu \cdot n_{\min} + h\nu \cdot k - W , \tag{6}$$

where $h\nu = 1.53$ [eV] is the IR photon energy from the Ti:Sa laser, $n_{\min} = 6$ is the minimal number of photons needed to ionize FLU with these photons (first ionization potential of FLU is 7.91±0.02 [eV]), and W is the desired work function.

The work function W itself is given by the following expression:

$$W = \mathrm{IP} + U_{\mathrm{p}} , \tag{7}$$

where IP is the ionization potential (IP $= 7.91 \pm 0.02$ [eV] for FLU, as mentioned above) and U_{p} is the pondermotive energy given as[S5–S7]

$$U_{\mathrm{p}} = \frac{e^2 F_0^2}{4 m_{\mathrm{e}} \omega^2} \ , \tag{8}$$

where $e = 1.602176634 \times 10^{-19}$ [C] is the elementary charge, F_0 is the pulse peak electric field strength (V/m in SI units), $m_{\mathrm{e}} = 9.1093837015 \times 10^{-31}$ [kg] is the electron mass, and ω is the angular frequency of the pulse (Hz in SI units).[S8] We can rewrite Equation 8 using the field peak intensity $I_0 = c\varepsilon_0 F_0^2/2$ (given in W/m^2 in SI units) and wavelength $\lambda = 2\pi \cdot c/\omega$ (given in m in SI units), where $c = 299792458$ [m/s] is the speed of light in vacuum and $\varepsilon_0 = 8.8541878128 \times 10^{-12}$ [C/(V·m)] is the vacuum electric permittivity).[S8] This gives us the following expression for the pondermotive energy (in eV):

$$U_{\mathrm{p}}\ [\mathrm{eV}] \ = \frac{e}{8\pi^2 c^3 \varepsilon_0 m_{\mathrm{e}}} I_0 \lambda^2 = 9.33729 \times 10^{-5} \times I_0[\mathrm{PW/cm^2}] \times (\lambda[\mathrm{nm}])^2 \ . \tag{9}$$

Substituting the peak power estimate made from laser pulse parameters ($I_0^{(\mathrm{l})} = 0.033$ [PW/cm^2]) to the pondermotive energy, we obtain the expected value of $U_{\mathrm{p}}^{(\mathrm{l})} = 2.02$ [eV], which is larger than the photon energy of the IR pulse (1.5 [eV]). This means that the zeroth-order band ($k = 0$) should not be observed, and the lowest order of ATI peak we see is for $k = 1$ (see Equation 6). From the linear fit of the electronic kinetic energies (see Figure S16), we obtain the value of workfunction $W = 9.94 \pm 0.03$ [eV]. From this fitted value of $W = 9.94$ [eV] and FLU's first IP $= 7.91$ [eV], we get experimental value of the $U_{\mathrm{p}} = 2.03$ [eV].

Upon substitution of $U_{\mathrm{p}} = 2.03$ [eV] to Equation 9 with IR laser wavelength ($\lambda = 810$ [nm]), we get an estimate for the peak intensity from the pondermotive shift of $I_0^{(\mathrm{p})} = 0.033[\mathrm{PW/cm^2}] = 3.3 \times 10^{13}$ [W/cm^2]. This value is the same as the peak power estimate made from laser pulse parameters ($I_0^{(\mathrm{l})} = 3.3 \times 10^{13}$ [W/cm^2]). Both estimates are prone to different biases: the laser-parameters-based value makes assumptions on the pulse shapes, while the pondermotive-shift-based value relies on the image calibration quality and is more shifted to the ensemble-averaged parameters. Nevertheless, the cancellation of errors apparently provided a consistent peak power estimation.

Using the experimental value of the pondermotive energy (Equations 8 and 9), we can get the Keldysh parameter γ, which characterizes the ionization regime, according to the expression[S9]

$$\gamma = \frac{\omega\sqrt{2 m_{\mathrm{e}} \cdot \mathrm{IP}}}{e F_0} = \sqrt{\frac{\mathrm{IP}}{2 U_{\mathrm{p}}}} \ . \tag{10}$$

With $I_0^{(\mathrm{final})} = 3.3 \times 10^{13}$ [W/cm^2] the $U_\mathrm{p} = 2$ [eV] according to expression 9. FLU's first, second, and third ionization potentials are 7.9/13.1/17.4 eV, respectively.[S10] This gives the following Keldysh parameters: $\gamma = 1.4/1.8/2.1$, respectively.

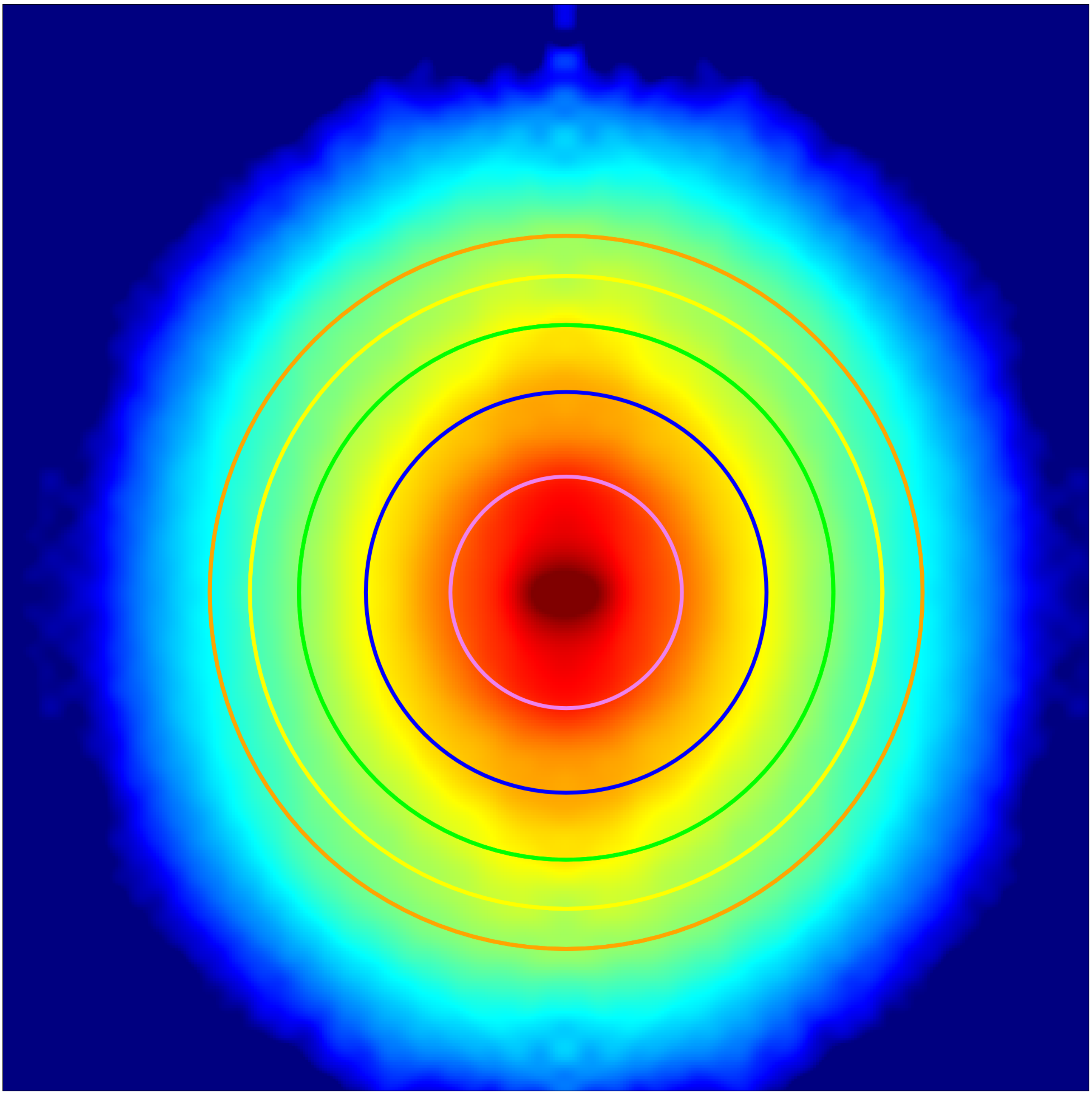

Figure S14 Abel inverted image from the raw image given in Figure S13. The raw image was symmetrized from the top left quadrant and then Gaussian-smooth before performing direct inversion. Note that the actual symmetry axis in Figure S13 is not exactly vertical but slightly tilted towards the left.

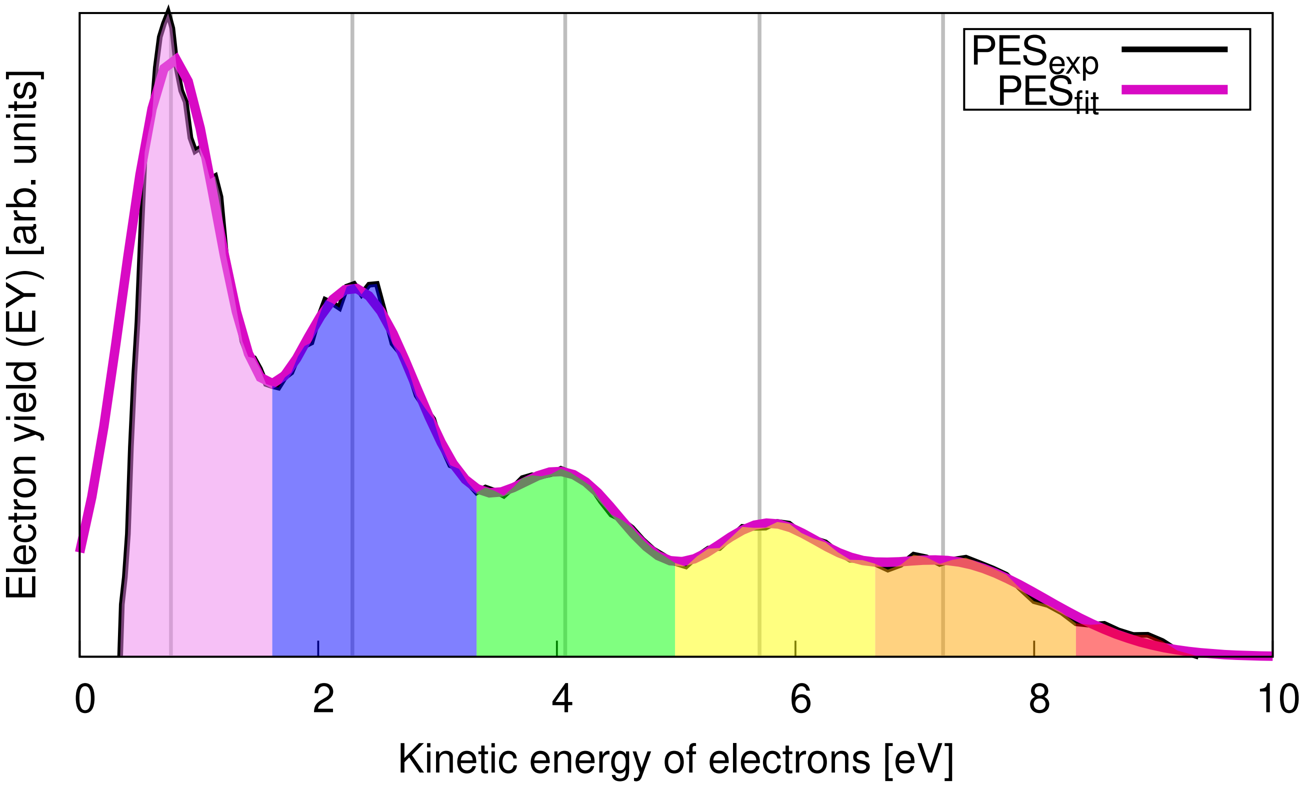

Figure S15 EY spectrum obtained from eVMI images, averaged over all pump-probe dependent data. The fit is given by Equation 5 with parameters of the fit given in Table S7.

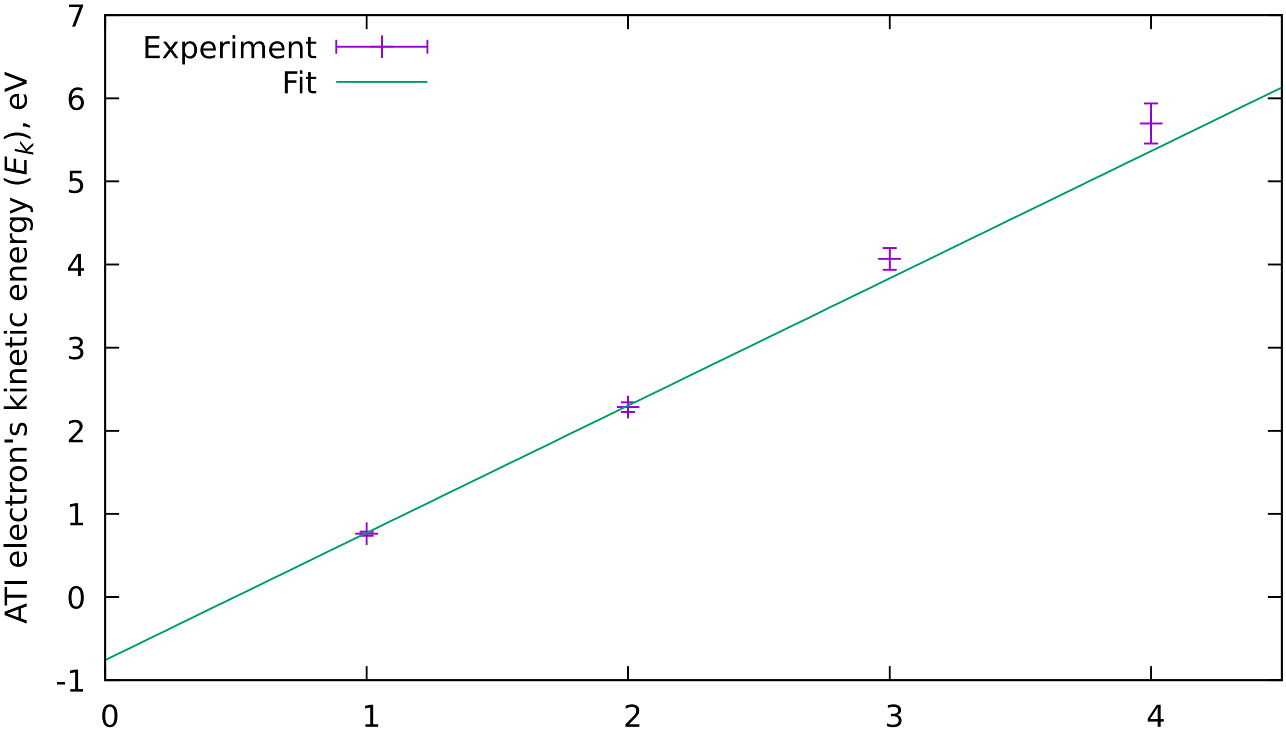

Figure S16 Fitting of the work function with Equation 6 from ATI peaks position given in Table S7.

6 Full PEPICOV map

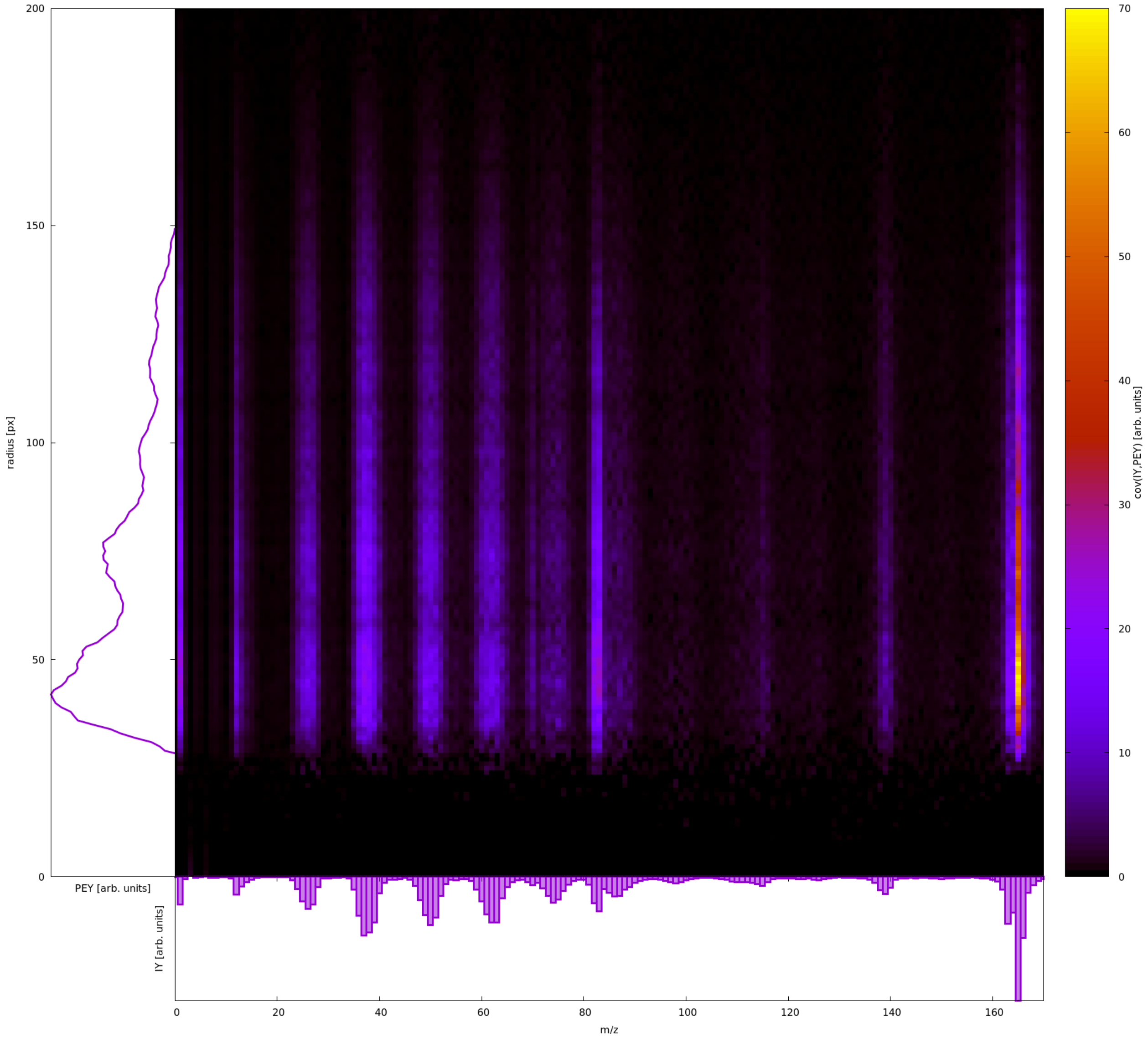

Figure S17 Full photoelectron-photoion covariance (PEPICOV) map of FLU. x-axis corresponds to the m/z, y-axis corresponds to the momentum of electrons (in pixels), color scale in the map provides the value of covariance between the ion yield for a given m/z with the photoelectron yield of a given momentum. The initial map was computed from the raw EY images, and then the electron axis of the map was Abel-inverted.

7 Quantum-chemical calculations of the reaction ${C_2}^{2+} \longrightarrow 2\,C^+$

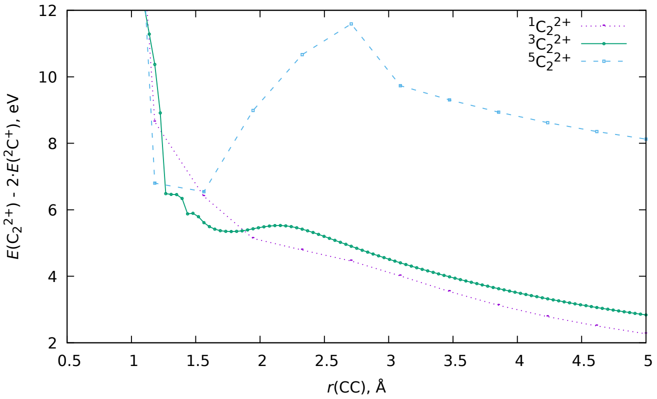

Figure S18 Dissociation curves of the ${C_2}^{2+}$ in singlet ($^1{C_2}^{2+}$), triplet ($^3{C_2}^{2+}$), and quintuplet ($^5{C_2}^{2+}$) states. Calculations were done at the CCSD(T)/aug-cc-pVTZ level of theory using the ORCA 5 package (version 5.0.4). The reference energy is the doubled energy of the doublet carbon monocations from Table S8.

Table S8 Results of quantum-chemical calculations for C^+ and ${C_2}^{2+}$ ions. Quantum chemical calculations were done at the CCSD(T)/aug-cc-pVTZ level of theory using the ORCA 5 package (version 5.0.4). The species are denoted as $^mC^+$ or $^mC_2^{2+}$, where m denotes multiplicity. Here, we provide electronic (equilibrium) energies (E_e) and optimized equilibrium interatomic distances (r(CC) for ${C_2}^{2+}$).

Specie	E_e [Ha]	r(CC) [Å]
$^2C^+$	-37.379380535269	–
$^4C^+$	-37.185822341003	–
$^3{C_2}^{2+}$	-74.564618952478	1.762
$^5{C_2}^{2+}$	-74.548881635953	1.349

The equilibrium energies of the ${C_2}^{2+}$ and C^+ species are given in Table S8, whilst the dissociation curves are provided in Figure S18. The lifetime of the metastable triplet ${C_2}^{2+}$ specie (τ) was computed using the following expression:[S11]

$$\tau^{-1} = \nu_{\text{ES}} \cdot \exp\left(\pi \cdot \left(\frac{\nu_{\text{ES}}}{\nu_{\text{TS}}} - \frac{2E_{\text{BH}}}{h\nu_{\text{TS}}}\right)\right) ,$$

where ν_{ES} is the harmonic vibrational frequency of the equilibrium state (ES) of the ${C_2}^{2+}$, ν_{TS} is the absolute value of the harmonic imaginary vibrational frequency of the transition state (TS) of ${C_2}^{2+}$ (at interatomic distance $r(\text{CC}) = 2.135$ Å), and E_{BH} is the barrier height (BH). The parameters of this equation obtained for the triplet ${C_2}^{2+}$ at the CCSD(T)/aug-cc-pVTZ level of theory are $\nu_{\text{ES}} = 526$ cm^{-1} (or 1.6×10^{13} Hz), $\nu_{\text{TS}} = 371$ cm^{-1}, and $E_{\text{BH}} = 828$ cm^{-1}. They result is $\tau = 0.9$ ns.

8 Approximation of the KER value for FLU tetracation dissociation through (2,2) channel

The kinetic energy release (KER) value for the dissociation of FLU^{2+} through (1,1) channel is reported to be in the range 2.40 to 2.60 eV.[S12] The total KER (TKER) can be thought to arise from the Coulombic repulsion between the two ions while dissociating (Equation 11).

$$\text{TKER} = k_\text{e}\frac{q_1 q_2}{r} \tag{11}$$

where k_e is Coulomb's constant. q_1 and q_2 are charges on the ions separated by distance r. For two dications, the TKER will scaled by a factor of 4. Therefore, TKER corresponding to the tetracation dissociation into two dications would approximately range from 9.60 to 10.40 eV. Using these values, one can calculate the value of the momentum of the participating fragments. For example, for the two fragment ions, namely $C_7H_x^+$ and $C_6H_y^+$, the TKER is reported to be 2.46 ± 0.04 eV. The momentum of two fragment ions in the (2,2) channel dissociation can be approximated as follows.

$$\text{TKER} = \frac{p_1^2}{2m_1} + \frac{p_2^2}{2m_2} \tag{12}$$

where p_1 and p_2 denote the momentum of two fragment dications with masses m_1 and m_2. Due to momentum conversion, $|p_1| = |p_2|$.

$$\text{TKER} = \frac{p_1^2}{2}\left[\frac{1}{m_1} + \frac{1}{m_2}\right] \tag{13}$$

Solving p_1 for TKER $= 2.46 \cdot 4 = 9.84$ eV, m_1, mass of $C_7H_x^{2+}$ peak, at 86 amu, and m_2, mass of $C_6H_y^{2+}$ peak, at 80 amu, we get $p_1 = 4.6 \times 10^{-22}$ kg·m·s^{-1}.

9 Peak intensities of various fragments in the power scans

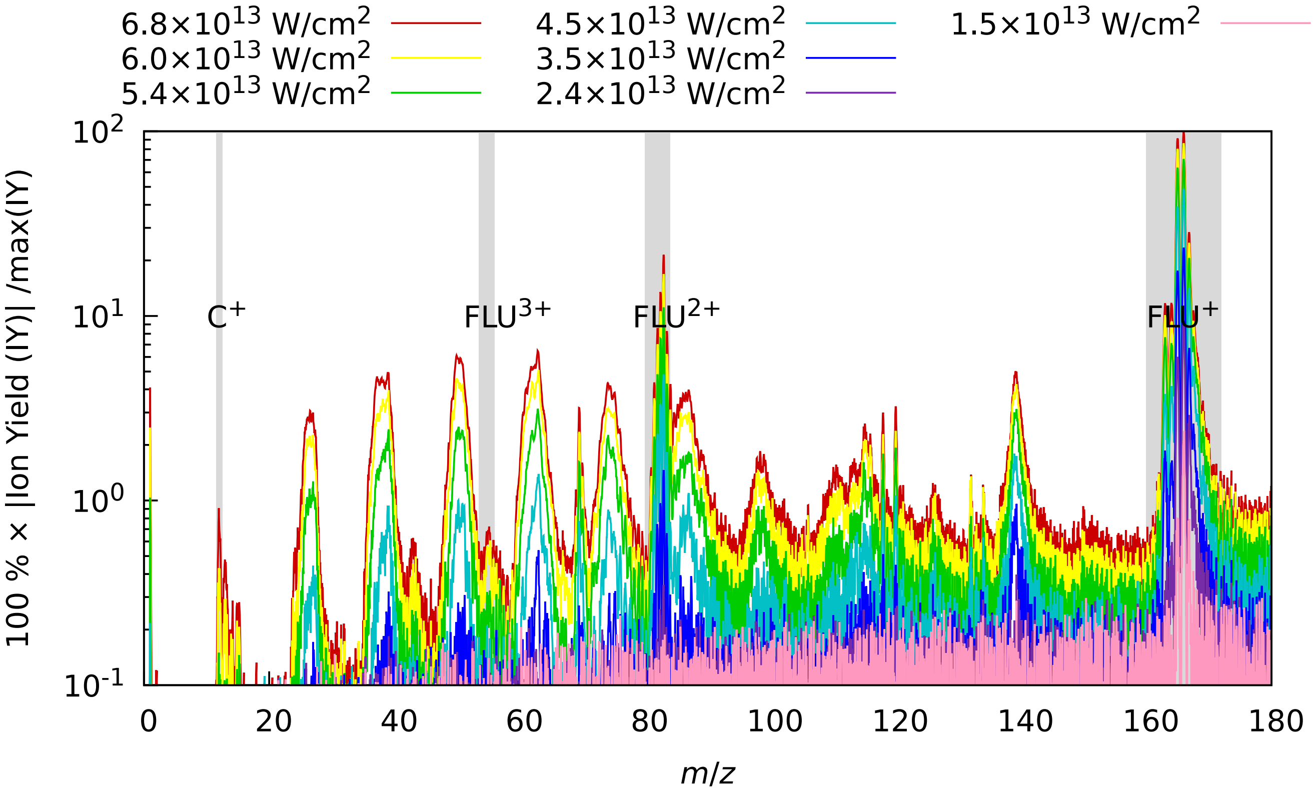

Figure S19 Experimental MS of FLU obtained with only the IR laser pulse for different intensities. The spectra were normalized to the maximum intensity peak of the FLU monocation ($C_{13}H_{10}{}^{+}$, $m/z = 166$) observed with the unattenuated data corresponding to a laser peak intensity of 3.1×10^{14} W/cm^2. The absolute values of the ion yields (|IY|) were taken to allow for a logarithmic scale since the baseline oscillates around zero signal and can have negative values. Gray-shaded areas highlight the four peaks of interest: C^+ ($m/z = 12$), FLU^{3+} ($m/z = 55.3$), FLU^{2+} ($m/z = 83$), and FLU^{+} ($m/z = 166$). Note that the logarithmic scale is used for the ion yield axis.

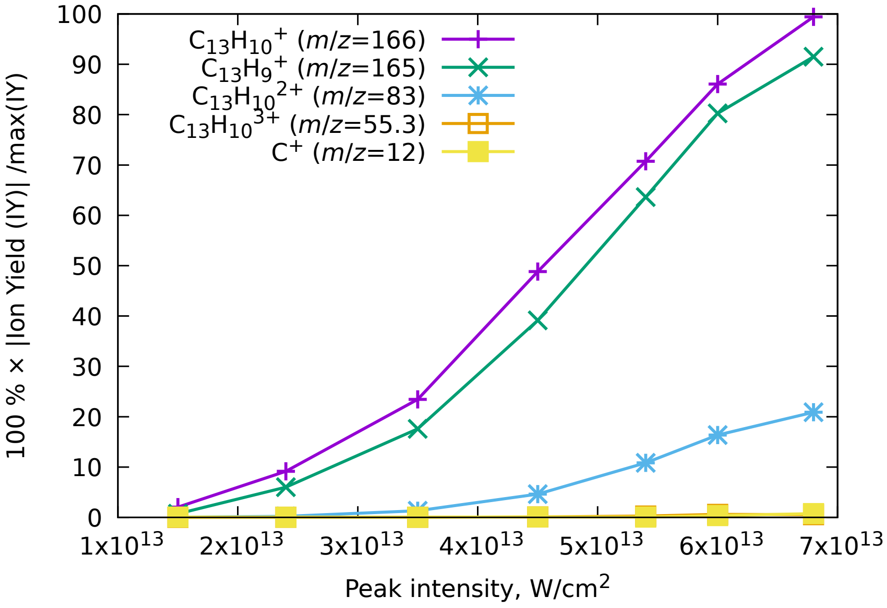

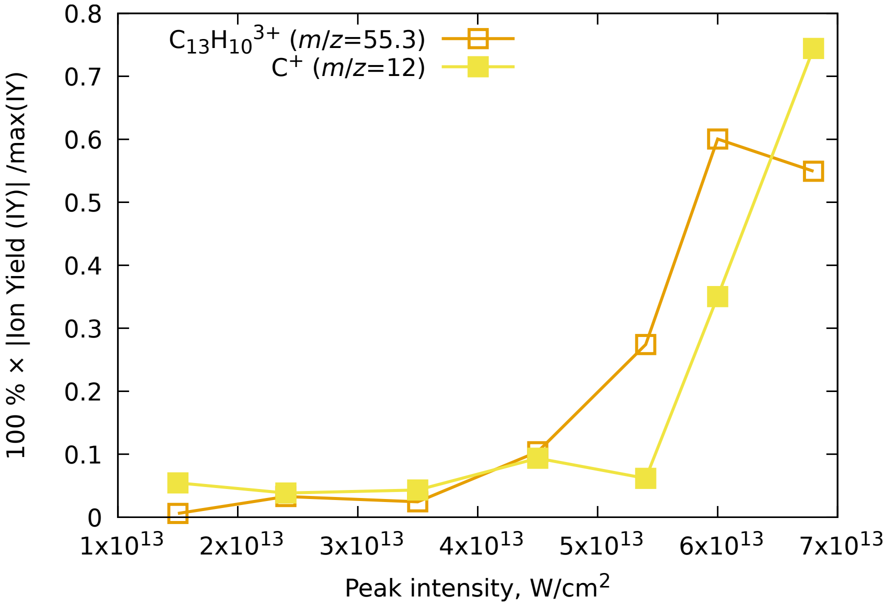

Figure S20 Intensities of selected peaks in the mass-spectra of FLU upon the mass scans: four parent ions ($C_{13}H_{10}^+$, $C_{13}H_9^+$, $C_{13}H_{10}^{2+}$, and $C_{13}H_{10}^{3+}$) and lowest mass fragment (C^+). Top figure: all peaks. Bottom figure: zoom into the low-intensity range.

References

(S1) Chopra, P. Astrochemically Relevant Polycyclic Aromatic Hydrocarbons Investigated using Ultrafast Pump-probe Spectroscopy and Near-edge X-ray Absorption Fine Structure Spectroscopy. Ph.D. thesis, Christian-Albrechts-Universität zu Kiel (Germany), 2022.

(S2) Tikhonov, D. S. MC^{3}Fitting. 2021; `https://gitlab.desy.de/denis.tikhonov/mcmcmcfitting`.

(S3) Tikhonov, D. S.; Garg, D.; Schnell, M. Inverse Problems in Pump–Probe Spectroscopy. *Photochem* **2024**, *4*, 57–110.

(S4) Garg, D. Electronic structure and ultrafast fragmentation dynamics of polycyclic aromatic hydrocarbons. Ph.D. thesis, Universität Hamburg (Germany), 2023.

(S5) Freeman, R. R.; Bucksbaum, P. H.; Milchberg, H.; Darack, S.; Schumacher, D.; Geusic, M. E. Above-threshold ionization with subpicosecond laser pulses. *Phys. Rev. Lett.* **1987**, *59*, 1092–1095.

(S6) Lin, K.; Eckart, S.; Hartung, A.; Trabert, D.; Fehre, K.; Rist, J.; Schmidt, L. P. H.; Schöffler, M. S.; Jahnke, T.; Kunitski, M.; Dörner, R. Photoelectron energy peaks shift against the radiation pressure in strong-field ionization. *Science Advances* **2022**, *8*, eabn7386.

(S7) Wang, R.; Zhang, Q.; Li, D.; Xu, S.; Cao, P.; Zhou, Y.; Cao, W.; Lu, P. Identification of tunneling and multiphoton ionization in intermediate Keldysh parameter regime. *Opt. Express* **2019**, *27*, 6471–6482.

(S8) Tiesinga, E.; Mohr, P.; Newell, D.; Taylor, B. CODATA Recommended Values of the Fundamental Physical Constants: 2018. **2021**,

(S9) Zheltikov, A. M. Keldysh parameter, photoionization adiabaticity, and the tunneling time. *Phys. Rev. A* **2016**, *94*, 043412.

(S10) Lee, J. W. L.; Tikhonov, D. S.; Chopra, P.; Maclot, S.; Steber, A. L.; Gruet, S.; Allum, F.; Boll, R.; Cheng, X.; Düsterer, S.; Erk, B.; Garg, D.; He, L.; Heathcote, D.; Johny, M.; Kazemi, M. M.; Köckert, H.; Lahl, J.; Lemmens, A. K.; Loru, D.; Mason, R.; Müller, E.; Mullins, T.; Olshin, P.; Passow, C.; Peschel, J.; Ramm, D.; Rompotis, D.; Schirmel, N.; Trippel, S.; Wiese, J.; Ziaee, F.; Bari, S.; Burt, M.; Küpper, J.; Rijs, A. M.; Rolles, D.;

Techert, S.; Eng-Johnsson, P.; Brouard, M.; Vallance, C.; Manschwetus, B.; Schnell, M. Time-resolved relaxation and fragmentation of polycyclic aromatic hydrocarbons investigated in the ultrafast XUV-IR regime. *Nature Communications* **2021**, *12*, 6107.

(S11) Tikhonov, D. S.; Rykov, A. N.; Grikina, O. E.; Khaikin, L. S. Gas phase equilibrium structure of histamine. *Phys. Chem. Chem. Phys.* **2016**, *18*, 6092–6102.

(S12) Lee, J. W. L.; Tikhonov, D. S.; Allum, F.; Boll, R.; Chopra, P.; Erk, B.; Gruet, S.; He, L.; Heathcote, D.; Kazemi, M. M.; Lahl, J.; Lemmens, A. K.; Loru, D.; Maclot, S.; Mason, R.; Müller, E.; Mullins, T.; Passow, C.; Peschel, J.; Ramm, D.; Steber, A. L.; Bari, S.; Brouard, M.; Burt, M.; Küpper, J.; Eng-Johnsson, P.; Rijs, A. M.; Rolles, D.; Vallance, C.; Manschwetus, B.; Schnell, M. The kinetic energy of PAH dication and trication dissociation determined by recoil-frame covariance map imaging. *Phys. Chem. Chem. Phys.* **2022**, *24*, 23096–23105.